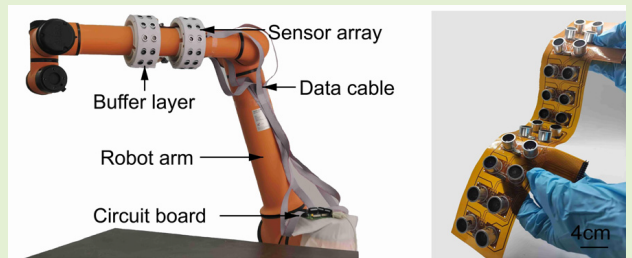


# Development of Flexible Highly Precise Ultrasonic Sensors for Safety Control in Human–Robot Collaboration

Yuan Li<sup>ID</sup>, Zhan Duan, Xuyang An, Xingyu Zhang, Jiahao Liang, Lijie Zhou, and Jia Zhang<sup>ID</sup>

**Abstract**—Proximity sensing is of great importance for robot control during human–robot collaboration (HRC). Commonly used machine vision sensors or photodetectors are subjected to the light block especially during close HRC, while capacitive sensors are easily interfered by the electromagnetic signal from the robot itself and its environment. Here, we present a flexible ultrasonic sensor system for proximity sensing, aiming to enhance safety controls during HRC. The sensor achieves an accuracy of 3 mm over a detection range of 510 mm. A minimum of 12 sensors are integrated into a flexible printed circuit board (FPCB), which functions as a wearable sensing system for a commercial robot. The sensor system effectively detects the position of objects around the robot in real time and covers all detection ranges in the detection plane at all angles, which is employed to control the robot in HRC. The manuscript delineates the sensors' performance, outlines the design of an ultrasonic sensor array for proximity sensing, and introduces a reliable method for secure and cooperative HRC control.

**Index Terms**—Flexible ultrasonic sensor, highly precise, human–robot collaboration (HRC), proximity sensor, safety control.



## I. INTRODUCTION

CURRENTLY, collaborative robots are extensively employed in various scenarios, including intelligent manufacturing [1], impatient healthcare and surgery [2], and personalized domestic help [3]. For these applications, the safety of both humans and robots is of paramount importance [4]. To make it a reality, various sensors are employed to gather environmental information, detect

Manuscript received 3 June 2024; revised 11 June 2024; accepted 15 June 2024. Date of publication 11 July 2024; date of current version 15 August 2024. This work was supported in part by the National Natural Science Foundation of China under Grant 52122513, in part by the National Key Research and Development Program of China under Grant 2022YFB3204700, in part by the Natural Science Foundation of Heilongjiang Province under Grant YQ2021E022, and in part by the Natural Science Foundation of Chongqing under Grant 2023NSCQ-MSX2286. The associate editor coordinating the review of this article and approving it for publication was Dr. Mert Torunbalci. (*Yuan Li and Zhan Duan contributed equally to this work.*) (*Corresponding authors: Lijie Zhou; Jia Zhang.*)

Yuan Li, Zhan Duan, Xuyang An, and Xingyu Zhang are with the State Key Laboratory of Robotics and System, Harbin Institute of Technology, Harbin 150080, China.

Jiahao Liang and Lijie Zhou are with the School of Mechanical and Power Engineering, Harbin University of Science and Technology, Harbin 150080, China (e-mail: ajie01265360@sina.com).

Jia Zhang is with the State Key Laboratory of Robotics and System, Harbin Institute of Technology, Harbin 150080, China, and also with Chongqing Research Institute, Harbin Institute of Technology, Chongqing 401120, China (e-mail: zhangjia@hit.edu.cn).

Digital Object Identifier 10.1109/JSEN.2024.3422169

obstacles' properties, and determine their positions [5]. Among these, proximity sensing emerges as a critical technology to prevent the collision between the robot and its environmental objects. In human–robot collaboration (HRC) [6], it is insufficient to rely solely on camera views or tactile sensors to avoid collisions. The proximity sensing capability integrated into the sensor system is vital.

For decades, many methods have been explored to detect an object approaching, which could be categorized by their operating principles, including capacitive [7], [8], [9], inductive [10], [11], optical [12], [13], and ultrasonic type [14]. The capacitors, inductors, and photodetector-based proximity sensors usually exhibit high sensitivity and rapid response [10], [12], [13], however, they are still vulnerable to structural and environmental factors. For example, a large electrode size is highly required to achieve high sensitivity in the long ranging, which is conflict to the high integration and small components [15]. Additionally, capacitive sensors are influenced by environmental conditions and object material characteristics [7], [8]. The inductive sensors are often susceptible to the conductivity of objects, electromagnetic interference, and nonlinear intervals [10]. A large detection of range (e.g., 300 mm) is achieved by using quite complex circuits [16]. The photoelectric proximity sensors are easily affected by the reflection characteristics of the object surface (color, reflectivity, roughness) [17], making it difficult to determine

object distance [18]. Meanwhile, objects with low reflection or black surfaces are found to be very difficult to detect because of the low reflected light [19]. Moreover, sensors might not detect the objects or may produce large deviations because of the small spatial resolution of the light beam, resulting in misjudgment [20], [21]. As a result, a large number of sensors are required to detect a wide-angle range. However, due to the small size of the sensors (e.g.,  $3 \times 4 \text{ mm}^2$ ) [22], achieving a larger detection angle imposes significant wiring challenges.

Recently, sensor fusion of two or more principles has been employed to realize object proximity perception and overcome each other's shortcomings [18], [23]. However, the distance range is still not large enough. Due to the inherent limitations of the sensor, there is a relatively large error in distance detection. A large range of perception needs more sensors, leading to complex integrated circuit wiring and difficulty in achieving real-time security perception [10]. Consequently, there are still challenges for the high-precision applications [24].

As an alternative, ultrasonic proximity sensors can overcome the above drawbacks, showing a long proximity distance with submillimeter resolution and being less susceptible to obstructions. Moreover, they provide higher reliability and stability across diverse application scenarios [25]. Nevertheless, ultrasonic sensors often have relatively complex structures and bulk volumes, making miniaturization and flexibility difficult without affecting performance. In addition, a single ultrasonic sensor has limited coverage of space because of the directional nature of ultrasonic waves. Therefore, a sensor array is required to cover all ranging angles in HRC.

Herein, we present a flexible ultrasonic sensor system that can accurately detect the distance between the robot and objects within a range of 510 mm with a ranging accuracy of 3 mm. A minimum of 12 sensors are integrated into a flexible printed circuit board (FPCB), which serves as a wearable sensing system for a commercial robot. The sensor system can effectively detect the position of objects around the robot in real-time without any dead angles in the detection plane, which is employed for the safety control of commercial robots in HRC.

## II. ULTRASONIC PROXIMITY SENSOR

### A. Principle of Ultrasonic Proximity Sensor

Ultrasonic sensors have been extensively used in noncontact measurement, distance ranging, and object recognition [26]. They all highly depend on the time and phase difference between the transmitted and received sound waves. For distance ranging in air, ultrasonic waves predominantly propagate through air in the form of longitudinal waves and reflect back from objects [27]. The wave can be depicted as the following equation:

$$A = A(x) \cos(\omega t + kx) = A_0 e^{-\alpha x} \cos(\omega t + kx) \quad (1)$$

where,  $A_0$  represents the initial amplitude,  $\alpha$  is the damping coefficient ( $\text{Np}/\text{m}$ ),  $\omega$  is the angular frequency of the ultrasonic signal ( $\text{rad}/\text{s}$ ),  $t$  is the propagation time of the ultrasonic wave in air (s),  $k$  is the wavenumber, and  $x$  is the distance of acoustic wave transmission. The damping coefficient and wavenumber

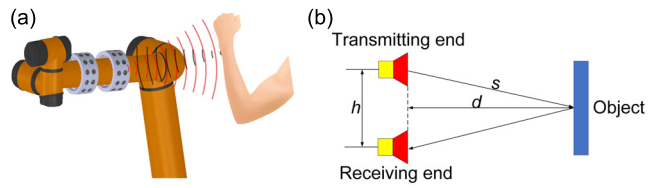


**Fig. 1.** Schematic of the ultrasonic proximity sensor for object ranging. (a) Diagram of measurement principle of the sensing system. (b) Model of ranging distance via TOF method.

can be expressed by the following equations:

$$\alpha = af^2 \quad (2)$$

$$k = 2\pi/\lambda \quad (3)$$

where,  $a$  represents the medium constant (in air,  $a = 2 \times 10^{-13} \text{ s}^2/\text{cm}$ ) and  $f$  is the frequency of the ultrasonic wave (Hz). Accordingly, there is a faster attenuation rate for higher frequency ultrasound, resulting in a quicker reduction in signal strength during propagation and thereby a shorter transmission distance. Additionally, high-frequency ultrasound is more susceptible to noise interference during propagation, resulting in a lower signal-to-noise ratio (SNR). Simultaneously, there is weaker reflection signal from objects especially for the small-sized ones at low-frequency ultrasound, resulting in reduced measurement accuracy [28]. As a result, the frequency is set at 40 kHz in our experiment to get a balance among ranging distance, reflected signal intensity, and measurement accuracy.

**Fig. 1(a)** schematically illustrates the distance measurement principle of the proximity sensing system equipped on the robot arm. The time-of-flight (TOF) method is employed to range the distance ( $d$ ) between the sensor and the reflection point on the target object [29]. Herein, the  $d$  is calculated as follows:

$$d = \sqrt{\left(\frac{1}{2}ct\right)^2 - \left(\frac{h}{2}\right)^2} \quad (4)$$

where,  $h$  is the center distance of the two ultrasonic transducers,  $t$  is the TOF, and  $c$  is the sound speed in air. To overcome the influence of the temperature on the sound speed in air, the  $c$  is rectified by the following equation:

$$c = \sqrt{\frac{rRT}{M}} \quad (5)$$

where,  $r$  represents the ratio of specific heat at constant pressure to specific heat at constant volume,  $R$  is the molar gas constant ( $8.31 \text{ J}/(\text{mol}\cdot\text{K})$ ),  $T$  is the thermodynamic temperature (K), and  $M$  is the molar mass of air ( $2.90 \times 10^{-3} \text{ kg/mol}$ ). As a result,  $c$  can be calculated by  $c = 0.607t + 331.5$ . Herein,  $t$  represents the actual temperature in air with unit of degree Celsius ( $^\circ\text{C}$ ).

### B. Sensor Unit Prototype and Circuit Design

**Fig. 2** schematically illustrates the structure of the designed ultrasonic transducer, which includes several components such as a conical disk, a vibrating metal plate, a piezoelectric

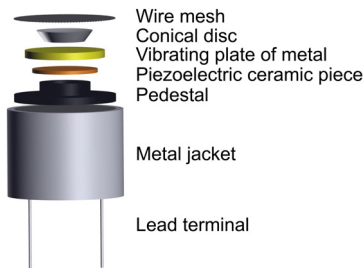


**Fig. 2.** Structural scheme of the ultrasonic sensor.

ceramic piece, and a pedestal. All of them are sealed in a metal jacket and covered by wire mesh.

Furthermore, the measurement unit circuit is designed to drive the ultrasonic transducer for transmitting and receiving signals. In brief, the microcontroller is employed to generate eight 40 kHz pulse signals to drive the transmitting transducers after voltage amplification. The reflected waves are received by the receiving transducers and then converted into electrical signals. In addition, the LM324 chip is utilized in the receiving circuit for amplification, filtering, and signal processing, through selection and other operations. Consequently, the signal quality is greatly enhanced to ensure the measurement accuracy.

### C. Performance of the Sensing Unit

After determining the proximity ultrasonic sensor and drive circuit, a comprehensive performance test and analysis were conducted and accumulated in Fig. 3. Fig. 3(a) shows the horizontal and vertical distributions of sound pressure levels, providing insights into the directional properties of the sound field. The directivity angle of the sound field is calculated to be 30° as the sound pressure level decreases to -3 dB according to the simulation results. The small directivity angle of the designed ultrasonic sensor guarantees a focused measurement range thereby enhancing ranging sensitivity and resolution, but it reduces the coverage area [30]. Herein, the directivity angle is set at 30° to achieve a balance between the measurement accuracy and coverage. Fig. 3(b) plots the sensor output voltage with respect to object distance at three azimuthal angles (0°, 15°, 30°) in reference to the central axis. Overall, the output voltage decreases as the object distance increases, while the maximum voltage is generally found in the central axis (0°) at the same distance [Fig. 3(b)]. The performance can be reasonably attributed to the sound pressure level distribution. Fig. 3(c) further confirms the sensor's detection angle range at diverse distances, which agrees well with the simulation result [Fig. 3(a)]. Fig. 3(d) plots the error distribution of the sensing unit at different distances of 5–40 cm. Overall, the error gradually decreases first and then increases as continuous increasing the distance. The maximum error remains within 3% (less than 3 mm) in all the measuring ranges under the static condition [Fig. 3(d)], indicating achieving a high measurement accuracy. In addition, Fig. 3(e) delineates the measurement error band under dynamic range, leading to the maximum dynamic error still within 3 mm. Finally, Fig. 3(f) plots the sensor outputs over 5000 cycles at room temperature, in which the inset

shows enlarged curves at the initial 200 cycles and the last 200 cycles. The quite uniform curves indicate a high stability of the designed sensor for the distance ranging [Fig. 3(f)].

## III. DESIGN OF SENSOR ARRAY AND VERIFICATION

### A. Design of Sensor Array

Considering the limitation of the ranging coverage of a sensor unit [Fig. 3(c)], the sensor array has to be developed to cover the all the spatial areas around the robot [31]. Fig. 4(a) and (b) depict the top view and stereo diagram of the ideal detection range in the simulation, respectively. A geometric model containing the conical sound field of the sensor unit and robot arm is established to determine the number of sensor units required to cover all angles around the robot arm [Fig. 4(c)]. Herein, the robot is the collaborative robot AUBO-i10. The parameter details are indexed in Fig. 4(c), where,  $R$  represents the radius (m) of robot arm at which the sensor is mounted,  $\theta$  is the angle (rad) between the center axis of the adjacent sensor units,  $L$  is the average width of a human arm, which is taken as 4 cm based on ergonomics,  $s$  is the minimum safe distance between the robot arm's links and a person (m),  $\alpha$  is the beam angle of the ultrasonic transducer (rad),  $n$  is the number of sensor units required around the circumference of the link,  $\omega_{\max}$  and  $\alpha_{\max}$  are the maximum angular velocity (rad/s) and angular acceleration (rad/s<sup>2</sup>) of the robot arm's joints, and  $\delta$  is the angle of joint rotation (rad).

Subsequently, the mathematical model is set up according to the geometric relationship of parameters and shown in the following equations:

$$R \sin \frac{\theta}{2} = \frac{L}{2} - \left( R + s - R \cos \frac{\theta}{2} \right) \tan \gamma \quad (6)$$

$$\gamma = \frac{\theta}{2} - \frac{\alpha}{2} \quad (7)$$

$$n = 2\pi / \theta \quad (8)$$

$$\omega_{\max}^2 = 2\alpha_{\max}\delta \quad (9)$$

$$s = \delta(L_1 + L_2). \quad (10)$$

According to (6)–(10), the minimum number of the ultrasonic sensor units is calculated to be 12 to cover all the specified areas. Each sensor unit contains a transmitting and receiving transducer. In this scenario, the sound field boundaries of adjacent sensor units are parallel to each other [Fig. 4(a)], which can guarantee the same gap between the sound fields of adjacent sensor units as the ranging distance increases [32]. When the flexible sensor is tightly installed around the robot arm radius ( $R = 58$  mm), the blind region is evenly distributed around the robotic arm and its width is 30.35 mm (less than the width of the human arm which is set at 4 cm). Consequently, the sensor consistently ensures the detection of humans and other objects, thereby enhancing the operational safety of the collaborative robot.

Considering the structure of the sensor array, all the sensor units reside in the same cross section of the robotic arm, which provides a highly effective perception effect in the plane [Fig. 3(d)]. In this scenario, it may only reflect off two ultrasonic transmitters if the size of the target object is too small (e.g., <4 cm), resulting in challenges for the

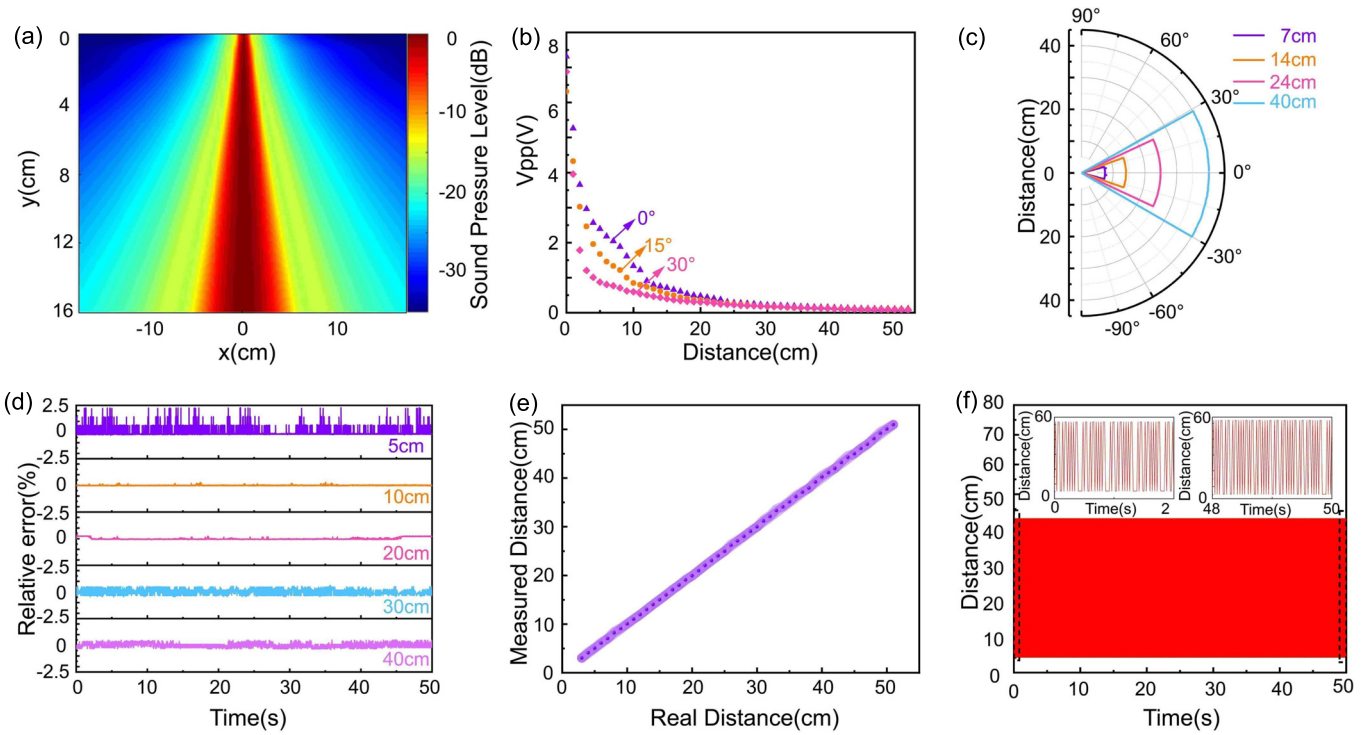


**Fig. 3.** Performance of single ultrasonic sensor. (a) Simulated sound pressure level distribution of the sensor. (b) Sensor output with respect to ranging distance at different angles reference to the central axis. (c) Angle measurement range. (d) Relative static error at the certain distances. (e) Absolute dynamic error in the distance range of 0–51 cm. (f) Cyclic stability of the sensor's output. Inset are enlarged curves at initial and last 200 cycles.

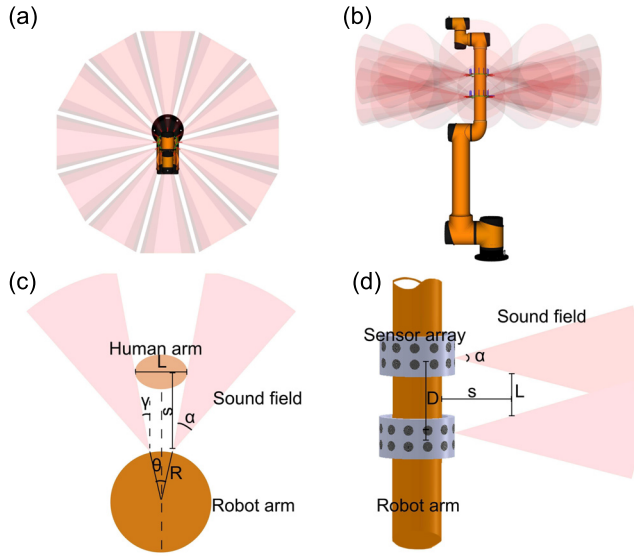


**Fig. 4.** Schematic of the sensor array. (a) Top view of detection range. (b) Stereoscopic diagram of detection range. (c) Sound field model of the sensor unit on the robot arm. (d) Sensor array distribution model around the robot arm.

sensor to accurately ascertain the object's position within the workspace. To address this problem, two flexible sensor arrays are mounted onto the same link of the robot arm [Fig. 4(d)]. With the overlapping sound fields of the two adjacent sensors on two arrays, a minimum of four sensor units can concurrently measure distance, facilitating the determination of the object's spatial position relative to the robot arm. To calculate

the parameter  $D$ , a geometric model is established as shown in Fig. 4(d). To ensure the 100% detection of the human body beyond the minimum safe distance ( $s$ ), the following relationship must be guaranteed

$$\frac{D - L}{2} = s \tan \frac{\alpha}{2}. \quad (11)$$

Accordingly,  $D$  is calculated to be 14.96 cm. Here, it is set at 14 cm to ensure full coverage of objects beyond the minimum safe distance.

### B. Design of Signal Acquisition System for Flexible Ultrasonic Sensor Array

The ultrasonic signal acquisition hardware system principally consists of an STM32F103ZET6 core circuit, a temperature compensation circuit, an RS232 serial communication circuit, a power supply circuit, and an interface for an ultrasonic sensor array. The STM32F103ZET6 core circuit orchestrates the system's overall operation. The temperature compensation is crucial to mitigate the impact of ambient temperature fluctuations on the velocity of ultrasonic waves. The RS232 serial port circuit facilitates data transmission and control by enabling communication with a supervisory computer.

Moreover, the sensor array was fabricated on the FPCB with a double-layer board-designed circuit part. The top layer is connected to an external power source through pin headers to provide a stable power supply for the sensor, while the bottom layer connects each sensor unit through wiring, enabling

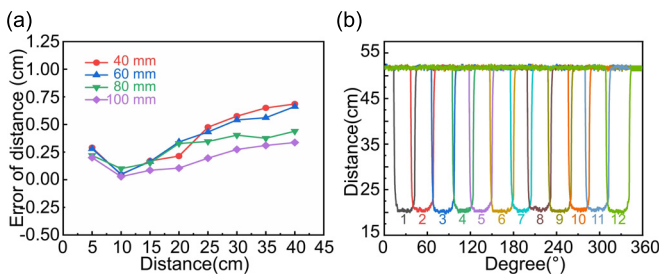


**Fig. 5.** (a) Absolute distance error with respect to ringing distance (in which the 40, 60, 80, and 100 mm, are the width of tested object). (b) The output of all the 12 sensors on one FPCB.

the transmission of sensor unit signals with dimensions of  $400 \times 105 \text{ mm}^2$ .

### C. Sensor Array Performance Analysis

The performance of the flexible ultrasonic sensor array was investigated in detail after the acquisition system was determined. Initially, a target was positioned at fixed distances ranging from 5 to 40 cm in step of 5 cm, while the width of the target varied from 4 to 10 cm. The data samples were collected in sets of 1000 points, and the average error for different widths and distances was calculated. Fig. 5(a) depicts the absolute error with respect to the range distance at various widths of the target object. The absolute error decreases first and then increases as the target object moves away from the sensor, leading to an inflection point at 10 cm. The tendency can be explained by two facts. When the detection range is close to the sensor (e.g.,  $<10 \text{ cm}$ ), the center distance of the two ultrasonic transducers is not negligible, and the TOF ranging principle produces an error. When the detection range is far from the sensor (e.g.,  $>10 \text{ cm}$ ), the reflected signal itself becomes weaker and the output fluctuates. Both conditions will result in a large absolute error [Fig. 5(a)]. Additionally, the width of the target object significantly affects measurement accuracy at a given distance. The smaller objects result in greater errors due to weaker signals in the whole sound field [Fig. 5(a)] [33].

To facilitate the detection of the human body, it is crucial to measure the sensor's detection range. To make it a reality, the sensor was affixed to a ring with the same radius as its mounting position on the mechanical arm and subsequently fixed on a turntable rotating at a constant speed. The target object with a width of 4 cm was placed 20 cm (which is the minimum safe distance in detection) away from the turntable. As the motor rotated at a slower speed, each unit sequentially detected the target object, allowing for the measurement of the blind zone width between adjacent sensors. The maximum detection distance is 51 cm [as shown in Fig. 5(b)]. Fig. 5(b) plots the output of all 12 sensors in one FPCB between 20 and 51 cm, where a distance beyond 51 cm indicates the object is undetected, while a distance of 20 cm confirms the presence of the target object. Additionally, the different color curves also indicate the object's presence sequentially as well as a certain degree of overlap. As a result, the sensor can detect objects at any angle in the detection plane when the width of the target object is beyond 4 cm.

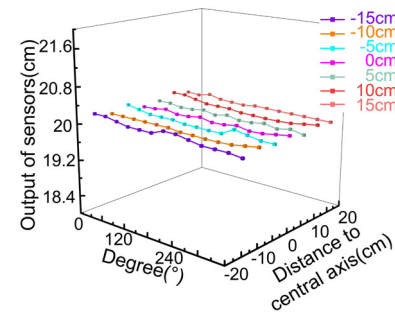


**Fig. 6.** Three-dimensional diagram of sensor axial test results.

We also conducted experiments on the detection range of the sensor along the axial direction of the robotic arm. Since the sound field angle of the sensor is  $30^\circ$ , we selected 12 points around the sensor to test the output result of the sensor to the object at the same distance. Up to 1500 tests were performed for each point, while the average value of the sensor output was recorded as the distance between the point and the sensor. At the same time, at each point parallel to the axial direction of the robot arm, the coverage degree of the sensor was detected from the central axis of the sensor array to both sides with a step length of 5 cm. The results are shown in Fig. 6. The results clearly demonstrate that the designed sensor system can achieve full coverage of  $360^\circ$  in the detection plane [Fig. 5(b)] and Fig. 6], and also has a large coverage space along the sensor's axial line (the coverage length is 35.2 cm when the distance is 20 cm from the axis).

## IV. EXPERIMENT AND VERIFICATION

To meet security requirements in HRC, we have designed a flexible sensor array. The previous experiments only verified the feasibility of the designed system. To further ensure its practicability, especially regarding security in HRC, additional experiments on the robot arm are necessary [34].

### A. Time-Sharing Start-Up and Positioning

First of all, there is interference in the propagation process of the one-transducer-one-receiver ultrasonic sensor [35]. Inevitably, crosstalk occurs between multiple sensing units. To overcome this drawback, we have implemented a group and time-division detection method. Using this method, the detection cycle of a single sensor array is segmented into four periods, each period lasting 3 ms. Twelve sensing units in one array are divided into three groups, each group corresponding to a microcontroller timer. Similarly, two different sensor arrays are also sampled in a time-division manner, which effectively reduces the effects of crosstalk and meets the real-time requirements.

And then, we need to use the distance data measured by the sensor to determine the position of the object relative to the robot arm. For this, a coordinate transformation is essential to convert coordinates between the sensor coordinate system and the robot coordinate system [36]. We utilized the TF library integrated into the robot operating system (ROS) to accomplish the transformation. Fig. 7 also illustrates the schematic of the

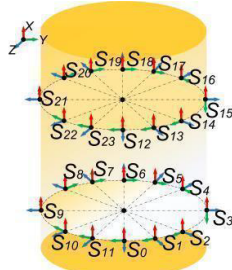


Fig. 7. Coordinate relationship diagram of sensor unit.

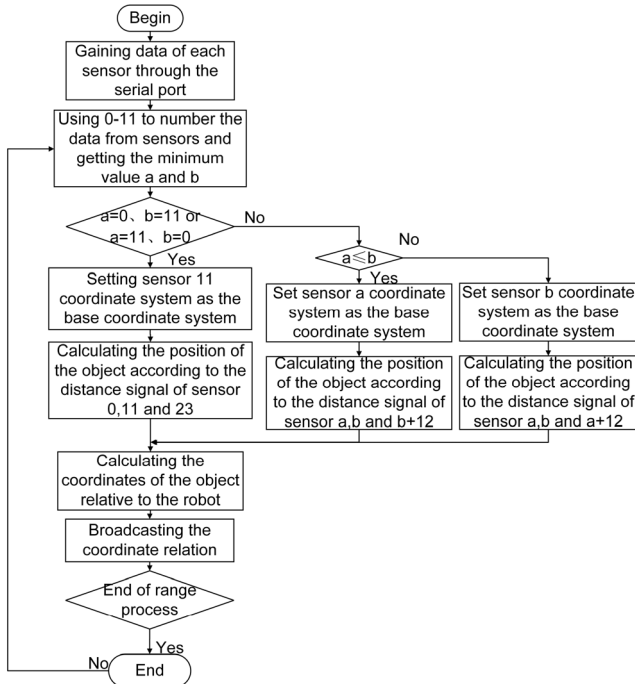


Fig. 8. Control flowchart of the flexible ultrasonic array.

coordinate relationships of each sensing unit, which shows the coordinates of each unit. This mechanism equips the robot with the ability to discern the location and orientation of objects in spatial space.

The detailed operational workflow is delineated in Fig. 8. The reflected wave received by four sensor units at least undergoes changes when the object is situated on the overlapping region of the acoustic fields of two ultrasonic sensor arrays. The orientation of the object is approximately determined by these sensor units. Subsequently, the three-sided positioning algorithm is employed to calculate the coordinates of the object relative to a specific ultrasonic sensor unit. Following this, the coordinate transformation relationships between each sensing unit and the robot coordinate system are used to calculate the spatial position of the object within the robot coordinate system. The data are then broadcast to other ROS nodes for subscription, thereby facilitating subsequent operations. During the process, the sampling period is highly related to the distance between the sensor and the object. The minimum value for 24 sensors is calculated to be about 54 ms to ensure the real-time performance of sensor system.

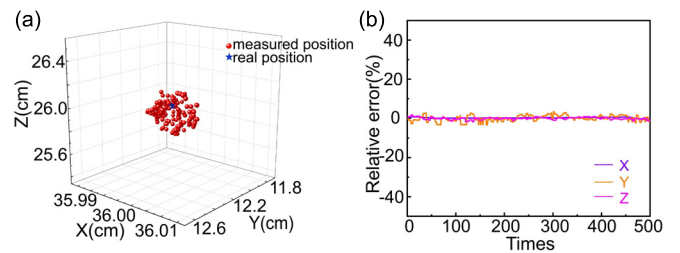


Fig. 9. (a) Three-dimensional coordinate diagram of test position and actual center point. (b) Relative errors on each axis.

Furthermore, the robot control experiments were conducted to validate the designed sensor system. During the experiment, four points were randomly selected within the acoustic field range of the sensor, and  $4 \times 4 \times 4 \text{ cm}^3$  objects were placed at these points. The three-sided positioning algorithm was then utilized to locate the test objects, aiming to assess the accuracy and reliability of the algorithm. To obtain the exact position of the object, it is necessary to calculate the coordinates of the center point of the object's reflection surface in the joint 3 coordinate system. Using the distance information obtained from the sensor, the results are obtained through the coordinate transformation. At each test point, up to 500 iterations were performed to attain more accurate results. The test positions and the actual center point results were plotted on a 3-D coordinate graph. Taking one of the datasets as an example [Fig. 9(a)], the performance of the positioning algorithm was evaluated by calculating the errors of each axis. The maximum errors are 0.7%, 3.2%, and 1.3% in the X, Y, and Z axes, respectively, which are quite small compared with previously reported results [Fig. 9(b)] [37]. The experimental findings confirm the high accuracy of the positioning algorithm, rendering it suitable for practical applications.

## B. Safety Stop Experiment

Upon verifying the security, the real-time performance is tested. Fig. 10(a) schematically illustrates the distribution of robot arm joints. Fig. 10(b) shows a series of pictures of the robot, which identifies its status during HRC. Fig. 10(c) plots the corresponding sensor output curves (The numbers of sensors in Fig. 10(c) correspond to the sensor numbers in Fig. 7 coordinate system). Initially, the sensor outputs are all approximately 51 cm which means no object around the sensor. Of course, the value (i.e., 51 cm) can be changed accordingly. As a human body suddenly appears within the range, the distance abruptly drops below 20 cm detection from the sensor units (i.e., No. 0, 1, 12, 13). Herein, the moving velocity of the robot arm is set at 0.45 rad/s. The robot arm promptly halts its planned action to avoid collision, which is evidenced by the angle change of joint 1 [Fig. 10(d)].

Subsequently, the detected distance increases again while the hand moves away from the robot. Meanwhile, the joint angle continues to change accordingly. This experiment demonstrates the efficacy of the robot arm's perception capabilities in detecting and responding to approaching objects.

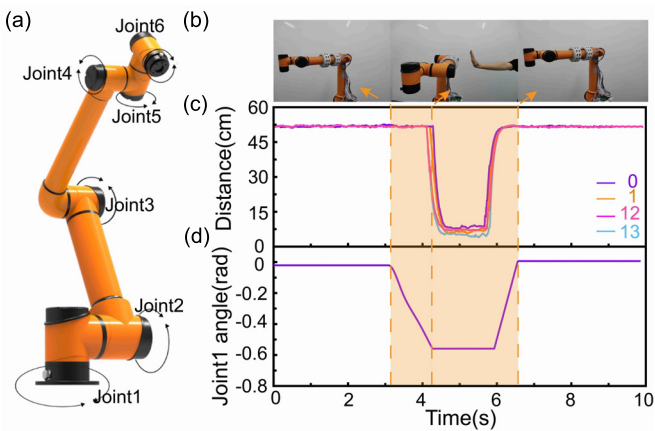


**Fig. 10.** (a) Joint of the robot arm. (b) Series pictures of robot during HRC. (c) Distance ranging results of the sensor system during HRC. (d) Output of the joint 1.

### C. Obstacle Avoidance Experiment

In order to further demonstrate the superiority of the flexible proximity sensing system, a robot obstacle avoidance test was designed. In the test, an ultrasonic sensor-based RRT-Connect algorithm was utilized to plan the trajectory of the robot. The robot arm was then controlled to execute active obstacle avoidance movement from the specified starting point to the target point in the environment with obstacles. Fig. 11(a) plots snapshots of the robot arm during obstacle avoidance. The corresponding sensor outputs and joint angles are recorded in Fig. 11(b) and (c), respectively.

The initial step in the operation of the robotic arm involves utilizing sensors to determine the positions of obstacles, as well as the starting and target points of movement. These points are subsequently integrated into the RRT-Connect tree as the root and target nodes, respectively. Utilizing a kinematic model and a collision detection algorithm, the robotic arm calculates the state of each node. It then generates a trajectory, assuming there are no obstacles impeding the path between the growth tree and the target tree. It is assumed that the absence of an obstacle is indicated by a sensor output value of 51 cm.

At the start of movement, the robotic arm assesses the presence of any impending obstacles through the sensor array located on connecting rod 3, with sensors 1 and 2 being in closest proximity to the obstacle. Following the execution of the RRT-Connect algorithm, the robotic arm initiates movement. As it approaches the obstacle, the sensor output from sensors 0, 1, 2, and 11, all within the obstacle detection range, begins to vary. This change reveals that sensors 1 and 2 are moving away from the object, while sensors 0 and 11 are gradually drawing closer, and the object still does not appear in the detective range of sensors 9 and 10. This observation aligns with the expected outcome.

Upon the completion and execution of the RRT-Connect tree planning, the robotic arm circumvents the obstacle in 8 s, with sensor 11 registering the closest proximity to the obstacle. Sensors 9 and 10 fail to detect any objects due to angular discrepancies. Following this 8-s interval, each joint maneuvers around the obstacle, leaving sensors 1 and 2 without any obstacles within their detection range, while

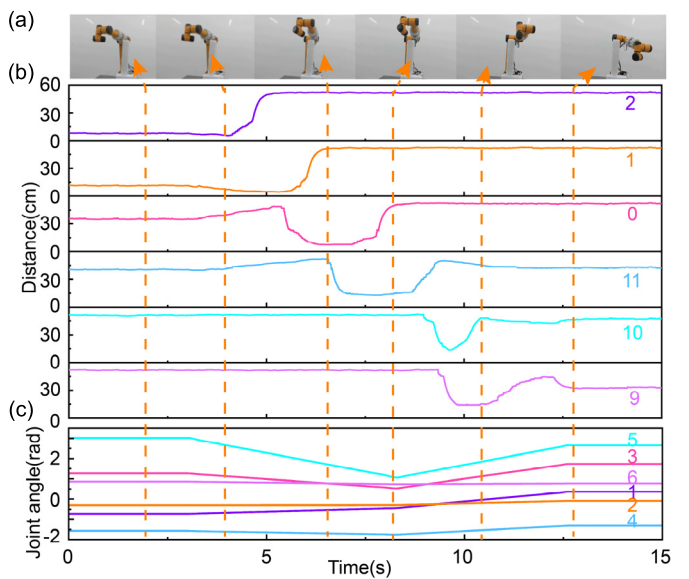


**Fig. 11.** Approaching process diagram and joint and sensor output during obstacle avoidance. (a) Motion position and attitude diagram of the robot arm. (b) Output of sensors during the processing of obstacle avoidance. (c) Output of joints 1–6 during the processing of obstacle avoidance.

sensors 0 and 11 initially draw closer to the object before distancing themselves as a result of joint 3's movement. Subsequently, the object enters the detection range of sensors 9 and 10.

In the latter stages of planning, sensors 0, 1, 2, and 11 are unable to detect any objects owing to the obstacle avoidance maneuver, whereas sensors 9 and 10 gradually achieve a stable distance as the robotic arm completes its motion. After 12.5 s, the robotic arm reaches the designated position, successfully concluding the obstacle avoidance planning.

As a result, the safety stop experiments demonstrate that the designed system possesses sufficient safety. It also exhibits a good real-time performance. These results effectively prove that the designed sensor system can provide reliable safety assurance in the process of HRC.

### V. CONCLUSION

In summary, we introduce a flexible ultrasonic sensor system for tailoring the collaborative robot. The sensing performances are comprehensively investigated, highlighting its advantages such as cost-effectiveness, ease of operation, high accuracy, and stability, which indicates it as a viable alternative to the effective proximity sensor in robot control. The developed sensor array system can be conformally integrated with the robot, and poised for versatile applications across various scenarios. It demonstrates remarkable accuracy with distance measurement precision of 3 mm on the robot arm, which ensures the safety and reliability of robot arm control. The sensor system is easy to integrate and can cover the detection plane in all directions and the detection space over a large range. In the future, we envision developing a flexible ultrasonic sensor system with more arrays to achieve full coverage of the robotic arm.

## REFERENCES

- [1] M. Faccio and Y. Cohen, "Intelligent cobot systems: Human-cobot collaboration in manufacturing," *J. Intell. Manuf.*, vol. 35, no. 5, pp. 1905–1907, May 2023.
- [2] F. Qi, M. Xiang, Y. Deng, W. Huang, and Y. Sun, "Application of da Vinci robot and thoracoscopy in radical lung cancer surgery," *J. Healthcare Eng.*, vol. 2022, pp. 1–8, Mar. 2022.
- [3] C. Di Napoli, G. Ercolano, and S. Rossi, "Personalized home-care support for the elderly: A field experience with a social robot at home," *User Model. User-Adapted Interact.*, vol. 33, no. 2, pp. 405–440, Jun. 2022.
- [4] Y. Li, Y. Luo, D. Chen, and Y. Xu, "An evaluation strategy of robot operation based on discrete workspace," in *Proc. IEEE Int. Conf. Real-Time Comput. Robot. (RCAR)*, Datong, China, Jul. 2023, pp. 602–607.
- [5] J. Liang, J. Wu, H. Huang, W. Xu, B. Li, and F. Xi, "Soft sensitive skin for safety control of a nursing robot using proximity and tactile sensors," *IEEE Sensors J.*, vol. 20, no. 7, pp. 3822–3830, Apr. 2020.
- [6] S. Robla-Gómez et al., "Working together: A review on safe human–robot collaboration in industrial environments," *IEEE Access*, vol. 5, pp. 26754–26773, 2017.
- [7] D. Čoko, I. Stančić, L. D. D. Rodić, and D. Čošić, "TheraProx: Capacitive proximity sensing," *Electronics*, vol. 11, no. 3, p. 393, Jan. 2022.
- [8] S. E. Navarro et al., "Proximity perception in human-centered robotics: A survey on sensing systems and applications," *IEEE Trans. Robot.*, vol. 38, no. 3, pp. 1599–1620, Jun. 2022.
- [9] Z. Liu, D. Chen, J. Ma, D. Jia, T. Wang, and Q. Su, "A self-capacitance proximity e-skin with long-range sensibility for robotic arm environment perception," *IEEE Sensors J.*, vol. 23, no. 13, pp. 14854–14863, Jul. 2023.
- [10] S. J. Moon, J. Kim, H. Yim, Y. Kim, and H. R. Choi, "Real-time obstacle avoidance using dual-type proximity sensor for safe human–robot interaction," *IEEE Robot. Autom. Lett.*, vol. 6, no. 4, pp. 8021–8028, Oct. 2021.
- [11] H. S. Han et al., "A highly sensitive dual mode tactile and proximity sensor using carbon microcoils for robotic applications," in *Proc. ICRA*, May 2016, pp. 97–102.
- [12] K. Qi, Z. Song, and J. S. Dai, "Safe physical human–robot interaction: A quasi whole-body sensing method based on novel laser-ranging sensor ring pairs," *Robot. Comput.-Integr. Manuf.*, vol. 75, Jun. 2022, Art. no. 102280.
- [13] Y. Liu, H. Xie, H. Wang, W. Chen, and J. Wang, "Distance control of soft robot using proximity sensor for beating heart surgery," in *Proc. IEEE/SICE Int. Symp. Syst. Integr. (SII)*, Dec. 2016, pp. 403–408.
- [14] Z. Tong et al., "An ultrasonic proximity sensing skin for robot safety control by using piezoelectric micromachined ultrasonic transducers (PMUTs)," *IEEE Sensors J.*, vol. 22, no. 18, pp. 17351–17361, Sep. 2022.
- [15] Y. Ding, H. Zhang, and U. Thomas, "Capacitive proximity sensor skin for contactless material detection," in *Proc. IEEE/RSJ Int. Conf. Intell. Robots Syst. (IROS)*, Oct. 2018, pp. 7179–7184.
- [16] T. D. Nguyen, T. Kim, J. Noh, H. Phung, G. Kang, and H. R. Choi, "Skin-type proximity sensor by using the change of electromagnetic field," *IEEE Trans. Ind. Electron.*, vol. 68, no. 3, pp. 2379–2388, Mar. 2021.
- [17] X. Lu, L. Sun, P. Jiang, and X. Bao, "Progress of photodetectors based on the photothermoelectric effect," *Adv. Mater.*, vol. 31, no. 50, Sep. 2019, Art. no. 1902044.
- [18] S. Tsuji and T. Kohama, "Proximity skin sensor using time-of-flight sensor for human collaborative robot," *IEEE Sensors J.*, vol. 19, no. 14, pp. 5859–5864, Jul. 2019.
- [19] D. Guo, P. Lancaster, L.-T. Jiang, F. Sun, and J. R. Smith, "Transmissive optical pretouch sensing for robotic grasping," in *Proc. IEEE/RSJ Int. Conf. Intell. Robots Syst. (IROS)*, Sep. 2015, pp. 5891–5897.
- [20] Y. Ding, F. Wilhelm, L. Faulhammer, and U. Thomas, "With proximity servoing towards safe human–robot-interaction," in *Proc. IEEE/RSJ Int. Conf. Intell. Robots Syst. (IROS)*, Nov. 2019, pp. 4907–4912.
- [21] P. Mittendorfer and G. Cheng, "Humanoid multimodal tactile-sensing modules," *IEEE Trans. Robot.*, vol. 27, no. 3, pp. 401–410, Jun. 2011.
- [22] G. B. Avanzini, N. M. Ceriani, A. M. Zanchettin, P. Rocco, and L. Bascetta, "Safety control of industrial robots based on a distributed distance sensor," *IEEE Trans. Control Syst. Technol.*, vol. 22, no. 6, pp. 2127–2140, Nov. 2014.
- [23] S. Tsuji and T. Kohama, "Proximity and contact sensor for human cooperative robot by combining time-of-flight and self-capacitance sensors," *IEEE Sensors J.*, vol. 20, no. 10, pp. 5519–5526, May 2020.
- [24] C. Glowa and T. Schlegl, "Ultrasound based object detection for human–robot collaboration," in *Proc. 6th Int. Conf. Intell. Robot. Appl. (ICIRA)*, 2013, pp. 84–95.
- [25] V. A. Zhmud, N. O. Kondratiev, K. A. Kuznetsov, V. G. Trubin, and L. V. Dimitrov, "Application of ultrasonic sensor for measuring distances in robotics," *J. Phys., Conf. Ser.*, vol. 1015, May 2018, Art. no. 032189.
- [26] A. Dimitrov and D. Minchev, "Ultrasonic sensor explorer," in *Proc. 19th Int. Symp. Electr. App. Technol. (SIELA)*, May 2016, pp. 1–5.
- [27] V. Ioana and A. N. Nordin, "Acoustic wave based MEMS devices for biosensing applications," *Biosensors Bioelectron.*, vol. 33, no. 1, pp. 1–9, Mar. 2012.
- [28] K. A. Wear, "The effects of frequency-dependent attenuation and dispersion on sound speed measurements: Applications in human trabecular bone," *IEEE Trans. Ultrason., Ferroelectr., Freq. Control*, vol. 47, no. 1, pp. 265–273, Jan. 2000.
- [29] J. C. Jackson, R. Summan, G. I. Dobie, S. M. Whiteley, S. G. Pierce, and G. Hayward, "Time-of-flight measurement techniques for airborne ultrasonic ranging," *IEEE Trans. Ultrason., Ferroelectr., Freq. Control*, vol. 60, no. 2, pp. 343–355, Feb. 2013.
- [30] A. Conjusteau, S. A. Ermilov, R. Su, H.-P. Brecht, M. P. Fronheiser, and A. A. Oraevsky, "Measurement of the spectral directivity of optoacoustic and ultrasonic transducers with a laser ultrasonic source," *Rev. Sci. Instrum.*, vol. 80, no. 9, Sep. 2009, Art. no. 093708.
- [31] Z. Qiu, Y. Lu, and Z. Qiu, "Review of ultrasonic ranging methods and their current challenges," *Micromachines*, vol. 13, no. 4, p. 520, Mar. 2022.
- [32] J. R. Llata, E. G. Sarabia, and J. P. Oria, "Three dimensional ultrasonic vision of surfaces for robotic applications," *IFAC Proc. Volumes*, vol. 31, no. 3, pp. 459–464, Mar. 1998.
- [33] S. Y. Shin and S. B. Choi, "Target speed sensing technique using dilation correlation of ultrasonic signal for vehicle," in *Proc. IEEE Sensors Appl. Symp. (SAS)*, Mar. 2019, pp. 1–5.
- [34] L. Fan, A. Song, and H. Zhang, "Development of an integrated haptic sensor system for multimodal human–computer interaction using ultrasonic array and cable robot," *IEEE Sensors J.*, vol. 22, no. 5, pp. 4634–4643, Mar. 2022.
- [35] O. A. Adamides, A. S. Modur, S. Kumar, and F. Sahin, "A time-of-flight on-robot proximity sensing system to achieve human detection for collaborative robots," in *Proc. IEEE 15th Int. Conf. Automat. Sci. Eng.*, Aug. 2019, pp. 1230–1236.
- [36] D. Whitney, E. Rosen, D. Ullman, E. Phillips, and S. Tellex, "ROS reality: A virtual reality framework using consumer-grade hardware for ROS-enabled robots," in *Proc. IEEE/RSJ Int. Conf. Intell. Robots Syst. (IROS)*, Madrid, Spain, 2018, pp. 1–9.
- [37] F. Aliew, "An approach for precise distance measuring using ultrasonic sensors," *Eng. Proc.*, vol. 24, no. 1, p. 8, 2022.



**Yuan Li** is currently pursuing the master's degree with the State Key Laboratory of Robotics and System, Harbin Institute of Technology, Harbin, China.

Her research interests include robot control and object shape and material recognition based on flexible ultrasonic sensors.



**Zhan Duan** is currently pursuing the Ph.D. degree with the State Key Laboratory of Robotics and System, Harbin Institute of Technology, Harbin, China.

His research interests include robotic arm compliance control and safe human–robot interaction based on proximity and tactile sensors.



**Xuyang An** is currently pursuing the Ph.D. degree with the State Key Laboratory of Robotics and System, Harbin Institute of Technology, Harbin, China.

His research interests include flexible electronic skin and its applications in wearable sensor.



**Lijie Zhou** is a Full Associate Professor with the School of Mechanical and Power Engineering, Harbin University of Science and Technology, Harbin, China.

Her research interests include robotic arm compliance control.



**Xingyu Zhang** is currently pursuing the master's degree with the State Key Laboratory of Robotics and System, Harbin Institute of Technology, Harbin, China.

His research interests include design of the flexible electronic skin and its applications in intelligent devices.



**Jiahao Liang** is currently pursuing the master's degree with the School of Mechanical and Power Engineering, Harbin University of Science and Technology, Harbin, China.

His research interests include electronic skin research for robot safety detection, human–robot cooperative safety, and collision detection.



**Jia Zhang** is a Full Professor with the State Key Laboratory of Robotics and System, Harbin Institute of Technology (HIT), Harbin, China.

He has published more than 70 articles in *Nature Electronics*, *Nature Communications*, *Advanced Materials*, with total citations of over 3000. He currently serves as the Editorial Board Member of *International Journal of Extreme Manufacturing* and *Micromachines*. His research interest is focused on the micro/nanofabrication of functional materials and structures for flexible electronics, including: flexible electronics for robotics tactile sensors, flexible and wearable devices, and 3-D printing for multimatials.